

Quantitative comparison of three-dimensional microstructure and determination of structural representative volume elements for the intact and compacted loess

Linxin Zhang

Chinese Academy of Sciences

Shengwen Qi (✉ qishengwen@mail.iggcas.ac.cn)

Chinese Academy of Sciences

Xiaokun Hou

Chinese Academy of Sciences

Songfeng Guo

Chinese Academy of Sciences

Zhiqing Li

Chinese Academy of Sciences

Guoliang Li

Chinese Academy of Sciences

Lina Ma

Chinese Academy of Sciences

Article

Keywords: three-dimensional microstructure, intact loess, compacted loess, CT technique, quantitative comparison, representative volume element (RVE)

Posted Date: April 11th, 2022

DOI: <https://doi.org/10.21203/rs.3.rs-1529647/v1>

License:  This work is licensed under a Creative Commons Attribution 4.0 International License.

[Read Full License](#)

Abstract

The pore structure is one of the most important properties of loess, which can directly affect the other properties such as water content, permeability and strength. It is of great significance to study the loess pore structure to ensure the safety and reliability of large-scale land creation and artificial infrastructure in the loess region. In this paper, the 3D pore characterization of intact loess and four kinds of compacted loess (with different dry densities) was investigated by microscale computed tomography. An efficient workflow is proposed to determine the structural representative volume elements of intact loess and compacted loess. Quantitative statistical analysis has shown that the heterogeneous level of the compacted loess is much greater than that of the intact loess on a microscopic scale. The intact loess has a higher porosity than the compacted loess, mainly because it has much more pores with an equivalent radius of 5~13 μm . And the pores of intact loess are more connected and more stable. As the compactness increases, pores of the compacted loess have been compressed, separated, or even disappeared. And pore disappearance of the small pores (<7 μm) mainly occurs under low compaction, while the compression and separation of medium (7~12 μm) and large pores (>12 μm) are dominant under high compaction. Moreover, the compacted loess will become more stable due to the present warm-humid climate.

1. Introduction

Loess, a grayish yellow or brownish yellow, clastic, highly porous, brittle Quaternary aeolian sediment, covers approximately 10% of the Earth's land surface^{1,2}. The Loess Plateau in mid-north China is the greatest bulk accumulation of loess on the earth³. It covers an area of 624,641 km² and spans seven provinces in China, making up 20% of arable land and supporting 17% of its population^{4,5}. As loess is a highly erosion-prone soil, the unique hilly-gully landscape was formed under the influence of human and natural activities for thousands of years⁶. Due to inappropriate soil conditions and multi-hazard scenarios, local farmers were in poverty as their efforts can hardly be paid off. The tense relationship between nature and human beings developed gradually.

With the development of economic construction in recent years, urban areas on the Loess Plateau have expanded rapidly, and the restriction of mountainous terrain on available construction land is becoming increasingly prominent⁷. To alleviate the nature-human tension and solve the shortage of construction land resources, local governments proposed the Mountain Excavation and City Construction (MECC) project⁸. In cities such as Chongqing, Yichang, Lanzhou and Yan'an, tens of square kilometers of new lands have been created. As one of the largest MECC projects, the amount of earthwork in Yan'an new district exceeded 600 million m³ to create 78.5 km² of flat land⁹. Dozens of hills with 100–150 m in height were removed to fill in valleys. Compaction, the most cost-effective way¹⁰, was used to improve the manual filling loess body. Its basic principle is to increase the density of loess by rolling or heavy tamping. The height of compacted loess filled in the valley could finally exceed 80 m. Besides the unprecedented scale, the coexistence of intact and compacted loess is another feature that differs from

previous projects. Recent work by engineers has established that the two kinds of foundations have obvious differences^{7,11-13}. The intact loess is uniform in nature and has good engineering geological conditions. By contrast, the compacted loess has a different degree of compressibility and collapsibility. These differences make the two kinds of foundations prone to uneven settlements, and ground fissure often occurs at the contact place. Hence, the comparative study of these two kinds of loess is of great value to the stability analysis of the site. This will be directly related to the long-term stability of this kind of large artificial loess project and whether it can meet the demand of urban construction.

Recently, a large number of scholars have carried out research on the properties of intact and compacted loess, and have found that compacted loess is quite different from intact loess^{11,13-16}. Many laboratory experiments proved have shown that despite the compaction measures, remolded loess still has collapsibility which can be even more serious than original loess¹⁷⁻²⁰. Besides, water retentions of the compacted loess and the intact loess are also different^{12,21}. Compared to re-compacted loess, intact loess exhibits a more pronounced hysteresis in the soil-water retention curve (SWRC) for low suctions. However, re-compacted loess exhibits larger hysteresis than intact loess for high suctions. It is worth mentioning that, the macro-level hydrological and mechanical properties of soils either in their compacted state or intact state is profoundly affected by the microstructure, especially the pore structure^{12,14,21-25}. As the compacted loess has a distinct pore-structure in comparison to the intact loess, it behaves differently from the intact loess in response to hydrological and mechanical change^{21,26,27}. Thus, qualitative and quantitative research on the soil pore structure of compacted loess and intact loess is of great significance for agricultural cultivation, water and soil conservation and engineering construction.

Mercury intrusion porosimetry (MIP) and scanning electron microscopy (SEM) are the most widely adopted techniques in such pore studies. The investigations have mainly concentrated on the determination of the plane morphology, two-dimensional characteristics of the loess pores, pore size distribution (PSD) and corresponding microstructural parameters²⁸⁻³². However, SEM can only obtain 2D images and the results are highly dependent on the choice of observing directions, which will result in non-unique shape descriptors for the pores³³. Because of the principle that forcing a non-wetting liquid (often mercury) to intrude into a material at high pressure to get the PSD, MIP is destructive so that the results may not be true^{34,35}, and it cannot directly visualize the pore structure¹¹. Fortunately, with the development of new observation apparatuses and processing technologies, X-ray computed tomography (CT) has been used to investigate the pore structure of loess in recent years^{1,26,36-40}. It can provide the images of each layer inside the sample without interfering with the test process and obtain 3D results²⁶. Nonetheless, due to the exorbitant price and the limited scanning pixels, researchers can only get 3D reconstructed pore structures in size of hundreds of microns, when the CT scan resolution is up to 1 μ m^{39,40}. And such high-resolution CT studies are extremely limited. Considering the heterogeneity of loess, especially compacted loess, the accuracy of such studies needs to confirm whether the tiny 3D pore structure can represent the properties of conventional size samples.

Representative volume element (RVE) is an important concept in the mechanics and physics of random heterogeneous materials^{41,42}. The RVE is usually regarded as a volume of heterogeneous material that is sufficiently large to be statistically representative of the microstructural heterogeneities⁴³. If the volume is relatively small, a slight increase in size may result in a notable change in characteristics. When the volume is larger than a critical value, the characteristics would no longer change with an increase in size. This critical value is called the representative volume element (RVE) size⁴⁴. Knowledge of the RVE size has been widely applied to accurate analyses of three-dimensional fractures network of jointed rock mass⁴⁵⁻⁴⁸. Similarly, it also contributes to the correct and accurate analysis of soil microstructure. This means that studies based on CT scans are representative if the tiny 3D volume corresponds to the RVE size. However, little research in this direction has been carried out.

Overall, the comparative studies on the 3D pore microstructure between intact loess and compacted loess based on the non-destructive CT scanning technology, especially at high resolution (1 μ m), is very limited. Moreover, whether such tiny three-dimensional pore structures are representative needs to be verified urgently.

In this paper, 3D pore microstructures of intact and compacted loess from the Loess Plateau were established based on serial CT images with a voxel size of 1 μ m³. Quantitative analysis and comparison were carried out to characterize the parameters of 3D structure volumes with different sizes. And geometrical RVE sizes of the microstructure of intact and compacted loess were determined. This research is expected to provide an in-depth and comprehensive understanding of the 3D pore geometrical characteristics of intact and compacted loess and insights into the study of the mechanical mechanism of loess behavior.

2. Methodology

2.1 Sampling and sample preparation

The soil materials used in this study were obtained from a slope of MBCC projects in Yan'an City, Shannxi, China (Fig. 1). Considering the obvious differences in material composition and microstructure of loess in different strata^{49,50}, all the samples used in the tests all come from the same place in the same stratum, the L6 layer of Middle Pleistocene (Q2) strata, to ensure the uniformity. The intact loess samples were well sealed by PVC pipe, plastic wrap and plastic tapes to avoid disturbance during the transportation. Primary physical parameters were determined according to the Chinese standard for soil test method (GB/T 50123 - 1999). The dry density and specific gravity were 1.54g/cm³ and 2.71, respectively. The liquid limit and plastic limit were 28.5% and 18.7%, respectively.

After sampling, the loose soil was dried at 100°C for more than 8 h, ground and sieved (passing through a 2-mm sieve). Then, 100g distilled water was sprayed onto 1000g dry soil, after which mixing continued until it obtained a uniform color and texture. And the well-mixed soil should be sealed in a resealable bag for more than 48 hours to reach moisture equilibrium. Subsequently, the soil was added into the sample-

making apparatus and compacted by the jack at the bottom for more than 40 seconds²⁶. The dry densities of compacted soil samples used in this study are 1.50g/cm³, 1.60g/cm³, 1.70g/cm³ and 1.80g/cm³, respectively.

Both the intact (YA-L6) and compacted (YA-1.5, YA-1.6, YA-1.7, YA-1.8) initial samples were then put in a dry place with constant temperature and ventilation for more than one month to meet the requirements of the CT scan. After air-drying, the samples were trimmed to cylindrical specimens (3mm in diameter and 5mm in height) by extremely thin and sharp blades. All the specimens were encased in a plastic tube to prevent disturbance (Fig. 2).

2.2 CT scanning and 3D reconstruction

In this study, a micro-CT device with high resolution (ZEISS Xradia520 Versa, Institute of Geology and Geophysics, Chinese Academy of Sciences, Beijing) was used to scan the specimens (Fig. 2). The voltage and current used for the image acquisition were 60 kV and 81 μ A, respectively. Given the scanning resolution of 1 μ m, 800 gray images were obtained for each specimen, and each image consisted of 1,002,820 (1015 \times 988) pixels with gray values in the range of 0-255. The 3D-cylindrical micro-samples can be obtained after the gray image combination (Fig. 3a). And the 3D cylindrical micro-samples were preprocessed by a Gaussian filter to clarify the particle boundary and facilitate the subsequent threshold selection (Fig. 3b).

2.3 Cube partition and data processing

For facilitating the subsequent pore segmentation and pore size statistics, a 600 μ m \times 600 μ m \times 800 μ m cube in the middle part of each 3D cylindrical micro-sample was selected as the region-of-interest (ROI) (Fig. 3c). Then each of these ROI cubes was cropped into different smaller cubes from 8 different positions. At each position, following a certain direction, a new bigger cube was generated while the side length increases every 100 voxels until the side length reaches the ROI cube size (Fig. 3d). The sub-volume selection scheme here can also be regarded as eight different grow regimes (self-similar regime) of a small cube to the original big cube^{51,52}.

For each cube (Fig. 4a), particles and pores were segmented in a semi-automatic way by using an interactive watershed tool and artificial selection. Then, the segmented pores were selected in 3D mode to generate new volume without the particle parts to obtain the 3D pore microstructure (Fig. 4b). Here, the porosity (P_o) is defined as the ratio of the number of pore voxels to the number of all voxels. As the connected pores and isolated pores could be distinguished (Fig. 4c, Fig. 4d), here the connected porosity (P_c) is defined as the ratio of the number of connected pore voxels to the number of all voxels, and the isolated porosity (P_i) is defined as the ratio of isolated pore voxels to the number of all voxels.

After pore space separation (Fig. 4e), the pores were generalized to form a pore network (Fig. 4f). By separation, the number of pores of (N_p) each cube could be obtained. And the Avizo XporeNetworkModeling Extension was required to access different statistics, such as pore volume, pore

area, pore equivalent radius, coordination number, throat equivalent radius and throat channel length. The pore volume is expressed as the number of voxels in a single pore. The pore area is expressed as the area of the total boundary in a single pore. The pore equivalent radius is expressed as the radius of a sphere whose volume is equal to the pore volume. The coordination number is defined as the number of throats connected to a given pore. The throat equivalent radius is defined as the radius of the thinnest contact position between two connected pores. The throat channel length is defined as the length of the throat between two connected pore centers. The median of pore volume, pore area, pore equivalent radius, throat channel length (M_V, M_A, M_R, M_L) and the average coordination number (C_n) were selected for the analysis. In addition, correlation accumulative curves were used for verification.

3. Results

3.1 Quantitative comparison of cubes of different sizes

Due to the limitation of the ROI size, the 8 cubes at different positions have a wide range of overlap when the side length is greater than $400\mu\text{m}^3$ (Fig. 3). Hence only two sizes of cubes, $200\mu\text{m}^3$ and $300\mu\text{m}^3$, were selected for analysis of mean and standard deviation. The results are shown in Fig. 5.

Considering the standard deviation can reflect the dispersion of a data set, the most interesting aspect of this graph is that P_o, P_c, P_i, N_p, C_n of the intact loess are more uniform than those of the compacted loess. And the dispersion of data has reduced when the side length increases, especially for the compacted loess. Even though YA-1.5 has a smaller dry density, the intact loess has greater porosity (P_o) and greater connected porosity (P_c) than the compacted loess (Fig. 5a, Fig. 5b), while its isolated porosity (P_i) is smaller than the compacted loess (Fig. 5c). And the intact loess has larger pore numbers (N_p) and larger average coordination numbers (C_n) (Fig. 5d, Fig. 5e).

By comparing the results of YA-1.5, YA-1.6, YA-1.7 and YA-1.8, it can be found that P_o and P_c of the compacted loess decrease as the dry density increases (Fig. 5a, Fig. 5b). P_i shows a trend of increasing first and then decreasing when the dry density increases (Fig. 5c). By contrast, N_p and C_n show a trend of decreasing first and then increasing when the dry density increases (Fig. 5d, Fig. 5e). It needs to be emphasized that all the turning points occurred when the dry density was $1.60\text{g}/\text{cm}^3$.

3.2 Determination of geometrical RVE

Figure 6 has shown part of the RVE analysis results based on different parameters of the intact loess (YA-L6) and the compacted loess (YA-1.5, YA-1.6, YA-1.7, YA-1.8). The x-axis represents the side length of cubes, while the y-axis represents the 3D parameters. As shown in Fig. 6, there are erratic fluctuations in the 3D parameters if the cube size is relatively small. And some lines begin to be steady as the cube size increases. Here the minimum X coordinate of the steady state is defined as the RVE side length. All the results based on different parameters at different positions are shown in Fig. 7. It can be observed that the results of different sub-volume selection schemes are different, even from the same loess sample.

And the difference is particularly evident in compacted loess. Besides, the RVE side lengths of the intact loess are generally smaller than those of the compacted loess. And as the dry density increases, the number of small RVE side lengths of the compacted loess has increased.

In this study, the biggest RVE side length based on nice parameters of eight sub-volume selection schemes should be taken as the geometrical RVE size of the original sample. Hence, the geometrical RVE sizes of YA-L6, YA-1.5, YA-1.6, YA-1.7 and YA-1.8 are $500\mu\text{m}^3$, $600\mu\text{m}^3$, $600\mu\text{m}^3$, $600\mu\text{m}^3$ and $600\mu\text{m}^3$, respectively. To verify the reliability of the results, correlation accumulative curves of the ROI cube and the geometrical RVE cubes have been compared. It is apparent from Fig. 8 that the cumulative curves of different geometrical RVE cubes are in good agreement with those of ROI cubes. Therefore, the current geometrical RVE sizes are trusted.

3.3 Quantitative statistical analysis based on RVE dimensions

For further understanding the 3D micro-structure difference of the intact and compacted loess, the RVE cube with a size of $600\mu\text{m}^3$ of each kind of loess was selected to carry out quantitative comparative statistics of pore equivalent radius distribution and throat equivalent radius distribution. For data consistency, the intact loess cube used here has the same size as the compacted loess's geometrical RVE cube. The results are shown in Fig. 9. Here the volume percentage means the ratio of the sum of the pore volumes of a particular equivalent pore radius to the sum of all the pore volumes. And the total volume means the sum of the pore volumes of a particular equivalent pore radius. Similarly, the length percentage means the ratio of the sum of the throat lengths of a particular equivalent throat radius to the sum of all the throat lengths. And the total length means the sum of the throat lengths of a particular equivalent throat radius.

From Fig. 9a and Fig. 9b, the intact loess has different pore equivalent radius distribution with the compacted loess. When the pore equivalent radius is less than $5\mu\text{m}$, the volume percentage of the intact loess is smaller than that of the compacted loess. But its total volume is slightly larger than the compacted loess, except for YA-1.8. When the pore equivalent radius is in the range of $5 \sim 13\mu\text{m}$, the total volume of the intact loess is much larger than that of the compacted loess. And its volume percentage tends to be close to that of compacted loess, especially the samples with higher dry density (YA-1.7), despite the dry density of the intact loess being closer to that of YA-1.5. When the pore equivalent radius is more than $13\mu\text{m}$, the volume percentage of the intact loess is gradually smaller than that of the compacted loess. And the total volume of the intact loess is smaller than that of the compacted loess under low compaction, while higher than that of the compacted loess under high compaction. Besides, as the only compacted loess sample whose dry density is less than that of the intact loess, YA-1.5 has a similar volume percentage and total volume with YA-L6 when the pore equivalent radius is less than $5\mu\text{m}$.

From Fig. 9c, there are no significant differences between the intact loess and the compacted loess on length percentage of throats at different equivalent throat radius. However, it is shown in Fig. 9d that, the

intact loess has a longer total length of throats than the compacted loess. Overall, the throats with the equivalent radius of 1–2 μm account for the largest proportion, both for the intact and the compacted loess.

What is also interesting in Fig. 9 is to compare the results of compacted loess with different dry densities (YA-1.5, YA-1.6, YA-1.7 and YA-1.8). As shown in Fig. 9a, when the pore equivalent radius is less than 7 μm , the volume percentage of the compacted loess increases with the increasing of dry density. When the pore equivalent radius is in the range of 7 ~ 15 μm , the volume percentage of the compacted loess increases first and then decreases with the increasing of dry density. When the pore equivalent radius is more than 15 μm , the volume percentage of the compacted loess decreases with the increasing of dry density, except for YA-1.8. Under some conditions, YA-1.8 can have a larger volume percentage. However, there are some differences in the total volume results. As shown in Fig. 9b, when the pore equivalent radius is less than 7 μm , the total volume of the compacted loess decreases first and then increases with the increasing of dry density. When the pore equivalent radius is in the range of 7 ~ 10 μm , the total volume decreases first in the case of low compactness, then increases rapidly with the increasing of dry density, and decreases again in the case of high compactness. When the pore equivalent radius is in the range of 10 ~ 12 μm , the total volume increases first and then decreases with the increasing of dry density. When the pore equivalent radius is more than 12 μm , the total volume decreases with the increasing of dry density, generally. Similarly, YA-1.8 can have a larger total volume under some conditions.

What's more, from Fig. 9c and Fig. 9d, it is obvious that the length percentage and the total length have decreasing trend with the increasing of dry density when the throat equivalent radius is more than 5 μm . When the throat equivalent radius is less than 2 μm , YA-1.8 has the largest length percentage and the largest total length, while YA-1.7 has the largest length percentage when the throat equivalent radius is in the range of 2–5 μm . And for the throats whose equivalent radius is in the range of 0–3 μm , the total length decreases first and then increases with the increasing of dry density.

4. Discussion

4.1 Comparison of intact loess and compacted loess

The afore mentioned results of standard deviations and RVE sizes (Fig. 5, Fig. 6, Fig. 7) have demonstrated that the heterogeneous level of the compacted loess is much greater than that of the intact loess on a microscopic scale.

Interestingly, by comparing the physical properties of natural loess and compacted loess, Zhang, et al.¹³ have found a similar pattern on a macroscopic scale. The difference of the heterogeneous level is closely related to the loess formation process of different loess. According to the hypothesis of eolian origin for loess, the formation process of intact loess is complex^{53–55}. The particles from the same source area are suspended under the combined action of upper westerly wind and near-surface wind. During

transportation, dust descends due to airflow and is deposited differently according to particle size. Therefore, the properties of sediments at the same location at the same age are basically the same, and the subsequent long-term evolution state is also basically the same. However, the formation process of compacted loess is done in a very short time. During sample remolding, an external force is needed to compact the sample into the required state. The external force is usually anisotropic and has a heterogeneous effect on the surface soil samples⁵⁶, which results in the anisotropic pore structure of remolded sample⁵⁷. According to the results in this study (Fig. 5, Fig. 7), it can be concluded that for the compacted loess, the degree of such pore heterogeneity decreases with the increase of dry density. A possible explanation for this might be that the particles have a certain optimal stacking state.

Another significant conclusion can be drawn from Fig. 5, that the pores of intact loess are more connected than those of the compacted loess. The total length results in Fig. 9d can also demonstrate this conclusion. This is because the long period of water seepage promotes the formation of connected pores in the natural intact loess^{1,58}. Thanks to the determination of geometrical RVE, it is confirmed that such tiny three-dimensional pore structures (no less $600\mu\text{m}^3$) are representative. There are also some interesting findings by the quantitative statistical analysis (Fig. 9a, Fig. 9b).

Firstly, unlike the previous study²¹ that dominant pores of the intact loess are smaller than the remolded loess, there is little difference in the dominant pores in this study. This discrepancy could be attributed to whether the results were obtained by MIP test or by CT scanning. Zhang, et al.²⁶ have found that the dominant pores from CT scanning are smaller than those from MIP test. Because X-ray CT is a nondestructive technique that does not interfere with or destruct the internal structure of soil. It means that the strength of pore structure of the compacted loess is less than that of the intact loess, hence the pores may be more obvious under high pressure intrusion by mercury compared. The high strength of the intact loess may be from the reprecipitate calcium carbonates and cements in long period of water infiltrating^{59,60}.

Secondly, the intact loess has much more pores whose equivalent radius is in the range of $5 \sim 13\mu\text{m}$ than the compacted loess (Fig. 9b). And this is the main reason for the intact loess's high porosity. Previous research has established that pores with a radius of less than $13\mu\text{m}$ are mostly occupied by combined water⁶¹. As the combined water cannot move freely under gravity, only the pores with radii larger than $13\mu\text{m}$ allow water to migrate³⁶. Therefore, the total volume of pores with a radius greater than $13\mu\text{m}$, instead of the porosity, is directly related to the permeability of loess. This means that the compacted loess under low compaction (YA-1.5, YA-1.6) may have higher permeability than the intact loess, even though the intact loess has a greater porosity. And the compacted loess under high compaction (YA-1.7, YA-1.8) may have lower permeability than the intact loess. Zhang, et al.¹³ has found similar results by the comparative study on the permeability of natural sedimentary loess and manual filling compacted loess from a site of MBCC projects.

4.2 Difference analysis of compacted loess with different dry density

According to the quantitative comparison in Fig. 5, one can find that the increase of compaction degree is accompanied by the shrinkage, separation and even disappearance of pores. Thanks to the determination of geometrical RVE, we can quantify the true volume and length value of pores rather than just the percentage content (Fig. 9).

By traditional percentage statistics, Zhang, et al.²⁶ has divided the pores of the compacted loess into three categories: large pores ($> 13\mu\text{m}$), medium pores ($8 \sim 13\mu\text{m}$) and small pores ($< 8\mu\text{m}$). They indicated that the large pores were firstly broken into medium pores and some small pores until the pore structure was close to the natural structure of the loess. Then a lot of medium pores were broken into small pores as the compactness was further increased. Similar results can also be obtained from Fig. 9a, but the three categories are large pores ($> 15\mu\text{m}$), medium pores ($7 \sim 15\mu\text{m}$) and small pores ($< 7\mu\text{m}$). This may be due to the difference in calculation methods of pore segmentation statistics during data processing^{62,63}. However, such conclusions cannot explain why N_p shows a trend of decreasing first and then increasing when the dry density increases (Fig. 5d).

Fortunately, the quantitative statistical analysis of the total volume of pores based on the pore equivalent radius has provided the evidence that explains the problem (Fig. 9b). Under low compaction, many small pores are compressed until they disappear, so that the total volume of the small pores ($< 7\mu\text{m}$) decreases. The medium pores and large pores are also compressed or even separated. The results have shown that the large pores are mainly compressed into the pores in the range of $10 \sim 12\mu\text{m}$. At this time, the number of pores increased by separation is less than the number of pores that disappeared, so the N_p shows a trend of decreasing. As the compactness increases, more pores are compressed and separated. A lot of pores in the range of $7 \sim 10\mu\text{m}$ appear. Here the number of pores increased by separation is much larger than the number of pores that disappeared. Under high compaction, the pores are further compressed and separated, especially for the pores whose equivalent radius is more than $7\mu\text{m}$. And more small pores ($< 7\mu\text{m}$) appear. As a result, the N_p shows a continuous upward trend. Besides, YA-1.8 sometimes has a larger volume percentage and a larger total volume when the pore equivalent radius is more than $12\mu\text{m}$. Because it is difficult to distinguish pore-throat segments under high compaction, so that some extremely narrow and long pores may be identified as large pores, resulting in large equivalent diameters.

To sum up, pores of the compacted loess have been compressed, separated, or even disappeared as the compactness increases. Pore disappearance mainly occurs under the condition of low compaction and small pores. Under the condition of high compactness, the compression and separation of medium and large pores are dominant. Considering the true volume results, the final partition scheme of the three pores is: large pores ($> 12\mu\text{m}$), medium pores ($7 \sim 12\mu\text{m}$) and small pores ($< 7\mu\text{m}$), based on the pore equivalent radius.

4.3 Inspiration of the micro-structural difference

Deng, et al.⁵⁰ have obtained the distribution of channel length for various loess and paleosol layers and indicate that the pore channel becomes slenderer with increasing stratum depth. In this study, one can find that the loess with high compaction has slenderer pore channels from Fig. 9c. This means that the compacted loess with high compaction is more similar to the older intact loess.

The difference between the intact loess and paleosol in permeability and water-bearing space is attributed to climatic difference and pedogenesis⁶⁴. The loess was mainly the dust deposits transported by the northerly wind of winter monsoons and also suffered to some extent from pedogenesis caused by weakened summer monsoons. It implies the history of a cold-dry climate with winter monsoon dominance. The paleosol accreted by the rather slow dust accumulation was closely related to strengthened summer monsoons. It implies the history of a warm-humid climate with summer monsoon dominance. Hao and Guo⁶⁵ have identified spatial changes in monsoon climate over the Loess Plateau in China at key glacial, interglacial, and interstadial intervals for the last 600kyr. The results indicate strong coherence between the interglacial periods and present-day precipitation and temperature patterns. Hence, the present-day climatic conditions are more conducive to the evolution of compacted loess towards the direction of paleosol.

Due to rainfall or the rise of groundwater level, the water content of compacted loess increases. With the downward migration of water, the horizontal tensile stress induced by matric suction and surface tension could easily cause the initial micropores to extend vertically⁶⁶, which facilitates the percolation of water. And the infiltrating water can dissolve soluble salts, causing transportation and reprecipitation of calcium carbonates and reinforcement of existing pores by cements^{1,59,67}. Besides, this long period of structural evolution can also reinforce the contacts of the clay particles⁶⁸. Hence, the compacted loess will become more stable.

5. Conclusion

In this paper, 3D pore microstructures of intact and compacted loess from the Loess Plateau were established based on micron-scale computed tomography. By quantitative analysis and comparison of the parameters of 3D structure volumes with different sizes, several important conclusions can be reached:

- 1) An efficient workflow for determinate the structural representative volume elements of intact loess and compacted loess is proposed. The geometrical RVE sizes of the microstructure of intact and compacted loess are $500\mu\text{m}^3$ and $600\mu\text{m}^3$, respectively.
- 2) The heterogeneous level of the compacted loess is much greater than that of the intact loess on a microscopic scale.
- 3) The pores of intact loess are more connected and more stable than those of the compacted loess.

- 4) The intact loess has a higher porosity than the compacted loess, mainly because it has much more pores with an equivalent radius of $5 \sim 13\mu\text{m}$.
- 5) As the compactness increases, pores of the compacted loess have been compressed, separated, or even disappeared. And pore disappearance of the small pores ($< 7\mu\text{m}$) mainly occurs under low compaction, while the compression and separation of medium ($7 \sim 12\mu\text{m}$) and large pores ($> 12\mu\text{m}$) are dominant under high compaction.
- 6) The compacted loess will become more stable due to the present warm-humid climate.

Declarations

Data availability

The data generated during and/or analyzed during the current study are available from the corresponding author on reasonable request.

Acknowledgements

The research is sponsored by the National Natural Science Foundation of China (Grant No. 41790442). And the authors wish to offer their gratitude and regards to the reviewers and the editors for their valuable comments.

Contributions

Shengwen Qi, Songfeng Guo conceived and designed the test. Linxin Zhang, Shengwen Qi, Lina Ma, Songfeng Guo, Zhiqing Li participated in the sampling process. Linxin Zhang, Lina Ma and Xiaokun Hou contributed laboratory experimental steps. Linxin Zhang, Guoliang Li contributed analytical steps. Shengwen Qi obtained financial support for the project. Linxin Zhang drafted the manuscript, and Shengwen Qi revised the manuscript. All authors discussed the article and gave their comments.

Additional Information

We confirm that this manuscript represents original work that has not been published elsewhere and is not under consideration by another journal for publication. All authors have approved the manuscript and agree with submission to Scientific Reports.

The authors declare no conflicts of interest.

References

1. Li, Y., He, S., Deng, X. & Xu, Y. Characterization of macropore structure of Malan loess in NW China based on 3D pipe models constructed by using computed tomography technology. *Journal of Asian Earth Sciences* **154**, 271-279, doi:10.1016/j.jseaes.2017.12.028 (2018).
2. Muhs, D. R., Prins, M. A. & Machalett, B. Loess as a Quaternary paleoenvironmental indicator. *Past Global Changes* **22**, 84-85, doi:10.22498/pages.22.2 (2014).
3. Derbyshire, E. Geological hazards in loess terrain, with particular reference to the loess regions of China. *Earth-Science Reviews* **54**, 231-260, doi:[https://doi.org/10.1016/S0012-8252\(01\)00050-2](https://doi.org/10.1016/S0012-8252(01)00050-2) (2001).
4. Zhang, T. Contention of Key Issues in China's Loess Plateau. *China Environmental Science Press (in Chinese)* (1993).
5. Hu, X. *et al.* Remote Sensing Characterization of Mountain Excavation and City Construction in Loess Plateau. *Geophysical Research Letters* **n/a**, e2021GL095230, doi:<https://doi.org/10.1029/2021GL095230> (2021).
6. Fu, B. *et al.* Hydrogeomorphic Ecosystem Responses to Natural and Anthropogenic Changes in the Loess Plateau of China. *Annual Review of Earth and Planetary Sciences* **45**, 223-243, doi:10.1146/annurev-earth-063016-020552 (2017).
7. Yao, Y., Zhang, Y., Ma, C., Zhao, Y. & Lv, G. Study on deformation of filling composite geological body in loess mountainous area. *Natural Hazards*, doi:10.1007/s11069-021-04998-x (2021).
8. Li, P., Qian, H. & Wu, J. Accelerate research on land creation. *Nature* **510**, 29-31 (2014).
9. Wu, Q., Jia, C., Chen, S. & Li, H. SBAS-InSAR Based Deformation Detection of Urban Land, Created from Mega-Scale Mountain Excavating and Valley Filling in the Loess Plateau: The Case Study of Yan'an City. *Remote Sensing* **11**, doi:10.3390/rs11141673 (2019).
10. Evstatiev, D. Loess improvement methods. *Engineering Geology* **25**, 341-366, doi:[https://doi.org/10.1016/0013-7952\(88\)90036-1](https://doi.org/10.1016/0013-7952(88)90036-1) (1988).
11. Ge, M., Li, N., Zhang, W., Zheng, J. & Zhu, C. Settlement behavior and inverse prediction of post-construction settlement of high filled loess embankment. *Chinese Journal of Rock Mechanics and Engineering* **36**, 745-753, doi:10.13722/j.cnki.jrme.2016.0014. (in Chinese). (2017).
12. Zhang, M. *et al.* Initial analysis on environmental effect of cutting hills to backfill ditch project on Loess Plateau — Take Yan'an New District as an example. *Geological Review* **65**, 1409-1421, doi:10.16509/j.georeview.2019.06.008. (in Chinese) (2019).
13. Zhang, L. *et al.* A comparative study on the physical properties of natural sedimentary loess and manual filling compacted loess. *Environmental Earth Sciences* **80**, 721, doi:10.1007/s12665-021-10047-4 (2021).
14. Jiang, M., Zhang, F., Hu, H., Cui, Y. & Peng, J. Structural characterization of natural loess and remolded loess under triaxial tests. *Engineering Geology* **181**, 249-260, doi:10.1016/j.enggeo.2014.07.021 (2014).
15. Liu, Z. *et al.* Collapsibility, composition, and microstructure of loess in China. *Canadian Geotechnical Journal* **53**, 673-686, doi: <https://doi.org/10.1139/cgj-2015-0285> (2016).

16. Wang, J.-D., Li, P., Ma, Y. & Vanapalli, S. K. Evolution of pore-size distribution of intact loess and remolded loess due to consolidation. *Journal of Soils and Sediments* **19**, 1226-1238, doi:10.1007/s11368-018-2136-7 (2018).
17. Zhang, G. Experimental study on collapsibility of compacted loess. *Water Resources and Hydropower Engineering*, 39-43, doi:<http://doi.org/10.13928/j.cnki.wrahe.1986.06.017> (1986).
18. Wu, S., Wu, J. & Dai, J. Study on collapsible deformation of compacted loess. *Journal of Xi'an Highway University* **17**, 1-3, doi:<http://doi.org/10.19721/j.cnki.1671-8879.1997.03.001> (1997).
19. Jia, M. Experimental study on collapsibility of compacted loess. *Shanxi Architecture*, 4-6,11, doi:<http://doi.org/10.13719/j.cnki.cn14-1279/tu.2000.01.002> (2000).
20. Chen, K.-s. & Sha, A.-m. Study of deformation characteristic of compacted loess *Rock and Soil Mechanics* **31**, doi:10.16285/j.rsm.2010.04.026. (in Chinese) (2010).
21. Hou, X. *et al.* Microstructure and soil-water retention behavior of compacted and intact silt loess. *Engineering Geology* **277**, 105814, doi:<https://doi.org/10.1016/j.enggeo.2020.105814> (2020).
22. Vanapalli, S. K., Fredlund, D. G. & Pufahl, D. E. The influence of soil structure and stress history on the soil–water characteristics of a compacted till. *Géotechnique* **49**, 143-159, doi:10.1680/geot.1999.49.2.143 (1999).
23. Ng, C. W. W., Sadeghi, H. & Jafarzadeh, F. Compression and shear strength characteristics of compacted loess at high suctions. *Canadian Geotechnical Journal* **54**, 690-699, doi:10.1139/cgj-2016-0347 (2016).
24. Ng, C. W. W., Mu, Q. Y. & Zhou, C. Effects of soil structure on the shear behaviour of an unsaturated loess at different suctions and temperatures. *Canadian Geotechnical Journal* **54**, 270-279, doi:10.1139/cgj-2016-0272 (2016).
25. Ng, C. W. W., Kaewsong, R., Zhou, C. & Alonso, E. E. Small strain shear moduli of unsaturated natural and compacted loess. *Géotechnique* **67**, 646-651, doi:10.1680/jgeot.16.T.013 (2017).
26. Zhang, L. *et al.* Three-dimensional pore characterization of intact loess and compacted loess with micron scale computed tomography and mercury intrusion porosimetry. *Scientific Reports* **10**, 8511, doi:10.1038/s41598-020-65302-8 (2020).
27. Rendell, H. M. Comparison between naturally consolidated and laboratory consolidated loess. *Engineering Geology* **25**, 229-233, doi:[https://doi.org/10.1016/0013-7952\(88\)90028-2](https://doi.org/10.1016/0013-7952(88)90028-2) (1988).
28. Grabowska-Olszewska, B. SEM analysis of microstructures of loess deposits. *Bulletin of the International Association of Engineering Geology - Bulletin de l'Association Internationale de Géologie de l'Ingénieur* **11**, 45-48, doi:10.1007/BF02635451 (1975).
29. Wang, J.-D., Li, P., Ma, Y. & Vanapalli, S. K. Evolution of pore-size distribution of intact loess and remolded loess due to consolidation. *Journal of Soils and Sediments* **19**, 1226-1238, doi:10.1007/s11368-018-2136-7 (2019).
30. Li, P., Xie, W., Pak, R. Y. S. & Vanapalli, S. K. Microstructural evolution of loess soils from the Loess Plateau of China. *Catena* **173**, 276-288, doi:<https://doi.org/10.1016/j.catena.2018.10.006> (2019).

31. Wu, S., Dai, J. & Peng, B. Study on microstructure and water seepage of compacted loess. *Journal of Xi'an Highway University* **18**, 19-22, doi:<http://doi.org/10.19721/j.cnki.1671-8879.1998.04.004> (1998).
32. Shao, X., Zhang, H. & Tan, Y. Collapse behavior and microstructural alteration of remolded loess under graded wetting tests. *Engineering Geology* **233**, 11-22, doi:<https://doi.org/10.1016/j.enggeo.2017.11.025> (2018).
33. Zhao, B. & Wang, J. 3D quantitative shape analysis on form, roundness, and compactness with μ CT. *powder Technol.* **291**, 262-275, doi:<https://doi.org/10.1016/j.powtec.2015.12.029> (2016).
34. Lawrence, G. P. Measurement of pore sizes in fine-textured soils: a review of existing techniques. *J. Soil Sci.* **28**, 527-540, doi:<https://doi.org/10.1111/j.1365-2389.1977.tb02261.x> (1977).
35. Romero, E. & Simms, P. H. Microstructure Investigation in Unsaturated Soils: A Review with Special Attention to Contribution of Mercury Intrusion Porosimetry and Environmental Scanning Electron Microscopy. *Geotechnical and Geological Engineering* **26**, 705-727, doi:<http://doi.org/10.1007/s10706-008-9204-5> (2008).
36. Wei, T., Fan, W., Yuan, W., Wei, Y.-n. & Yu, B. Three-dimensional pore network characterization of loess and paleosol stratigraphy from South Jingyang Plateau, China. *Environ Earth Sci.* **78**, doi:<http://doi.org/10.1007/s12665-019-8331-z> (2019).
37. Yu, B., Fan, W., Dijkstra, T. A., Wei, Y. N. & Deng, L. S. Heterogeneous evolution of pore structure during loess collapse: Insights from X-ray micro-computed tomography. *Catena* **201**, 105206, doi:<https://doi.org/10.1016/j.catena.2021.105206> (2021).
38. Yu, B. *et al.* X-ray micro-computed tomography (μ -CT) for 3D characterization of particle kinematics representing water-induced loess micro-fabric collapse. *Engineering Geology* **279**, 105895, doi:<https://doi.org/10.1016/j.enggeo.2020.105895> (2020).
39. Wei, Y.-n., Fan, W., Yu, N., Deng, L.-s. & Wei, T. Permeability of loess from the South Jingyang Plateau under different consolidation pressures in terms of the three-dimensional microstructure. *Bulletin of Engineering Geology and the Environment* **79**, 4841-4857, doi:10.1007/s10064-020-01875-y (2020).
40. Wei, Y.-n., Fan, W., Yu, B., Deng, L.-s. & Wei, T. Characterization and evolution of three-dimensional microstructure of Malan loess. *Catena* **192**, 104585, doi:<https://doi.org/10.1016/j.catena.2020.104585> (2020).
41. Bargmann, S. *et al.* Generation of 3D representative volume elements for heterogeneous materials: A review. *Progress in Materials Science* **96**, 322-384, doi:<https://doi.org/10.1016/j.pmatsci.2018.02.003> (2018).
42. Xu, W., Sun, X., Li, D., Ryu, S. & Khaleel, M. A. Mechanism-based representative volume elements (RVEs) for predicting property degradations in multiphase materials. *Computational Materials Science* **68**, 152-159, doi:<https://doi.org/10.1016/j.commatsci.2012.10.026> (2013).
43. Kanit, T., Forest, S., Galliet, I., Mounoury, V. & Jeulin, D. Determination of the size of the representative volume element for random composites: statistical and numerical approach. *International Journal of Solids and Structures* **40**, 3647-3679, doi:[https://doi.org/10.1016/S0020-7683\(03\)00143-4](https://doi.org/10.1016/S0020-7683(03)00143-4) (2003).

44. Zhang, W. *et al.* Determination of Geometrical and Structural Representative Volume Elements at the Baihetan Dam Site. *Rock Mechanics and Rock Engineering* **45**, 409-419, doi:[10.1007/s00603-011-0191-0](https://doi.org/10.1007/s00603-011-0191-0) (2012).
45. Min, K.-B. & Jing, L. Numerical determination of the equivalent elastic compliance tensor for fractured rock masses using the distinct element method. *International Journal of Rock Mechanics and Mining Sciences* **40**, 795-816, doi:[https://doi.org/10.1016/S1365-1609\(03\)00038-8](https://doi.org/10.1016/S1365-1609(03)00038-8) (2003).
46. Esmaili, K., Hadjigeorgiou, J. & Grenon, M. Estimating geometrical and mechanical REV based on synthetic rock mass models at Brunswick Mine. *International Journal of Rock Mechanics and Mining Sciences* **47**, 915-926, doi:<https://doi.org/10.1016/j.ijrmms.2010.05.010> (2010).
47. Zhang, W., Chen, J., Chen, H., Xu, D. & Li, Y. Determination of RVE with consideration of the spatial effect. *International Journal of Rock Mechanics and Mining Sciences* **61**, 154-160, doi:<https://doi.org/10.1016/j.ijrmms.2013.02.013> (2013).
48. Zhang, W. *et al.* Determination of Representative Volume Element Considering the Probability that a Sample Can Represent the Investigated Rock Mass at Baihetan Dam Site, China. *Rock Mechanics and Rock Engineering* **50**, 2817-2825, doi:[10.1007/s00603-017-1248-5](https://doi.org/10.1007/s00603-017-1248-5) (2017).
49. Lei, X. The types of loess pores in China and their relationship with collapsibility. *Sci. Chin. (Ser.B)* **31**, 1398-1411 (1988).
50. Deng, L. *et al.* Quantitative Research and Characterization of the Loess Microstructure in the Bai Lu Tableland, Shaanxi Province, China. *Advances in Civil Engineering* **2020**, 3681382, doi:[10.1155/2020/3681382](https://doi.org/10.1155/2020/3681382) (2020).
51. Wu, H., Zhou, Y., Yao, Y. & Wu, K. Imaged based fractal characterization of micro-fracture structure in coal. *Fuel* **239**, 53-62, doi:<https://doi.org/10.1016/j.fuel.2018.10.117> (2019).
52. Wu, H., Yao, Y., Zhou, Y. & Qiu, F. Analyses of representative elementary volume for coal using X-ray μ -CT and FIB-SEM and its application in permeability predication model. *Fuel* **254**, 115563, doi:<https://doi.org/10.1016/j.fuel.2019.05.146> (2019).
53. Kukla, G. & An, Z. Loess stratigraphy in Central China. *Palaeogeography, Palaeoclimatology, Palaeoecology* **72**, 203-225, doi:[https://doi.org/10.1016/0031-0182\(89\)90143-0](https://doi.org/10.1016/0031-0182(89)90143-0) (1989).
54. Rutledge, E. M., Guccione, M. J., Markewich, H. W., Wysocki, D. A. & Ward, L. B. Loess stratigraphy of the Lower Mississippi Valley. *Engineering Geology* **45**, 167-183, doi:[https://doi.org/10.1016/S0013-7952\(96\)00012-9](https://doi.org/10.1016/S0013-7952(96)00012-9) (1996).
55. Muhs, D. R. *Loess and its geomorphic, stratigraphic and paleoclimatic significance in the Quaternary*. Vol. 11 149-183 (American Society of Civil Engineers, 2013).
56. Ishibashi, I. & Hazarika, H. Soil Mechanics Fundamentals and Applications. *Archivio Italiano Di Chirurgia* **92**, 98-107 (2015).
57. Wang, H., Qian, H. & Gao, Y. Characterization of macropore structure of remolded loess and analysis of hydraulic conductivity anisotropy using X-ray computed tomography technology. *Environmental Earth Sciences* **80**, 197, doi:[10.1007/s12665-021-09405-z](https://doi.org/10.1007/s12665-021-09405-z) (2021).

58. Verachtert, E., Eeckhaut, M. V. D., Poesen, J. & Deckers, J. Factors controlling the spatial distribution of soil piping erosion on loess-derived soils: A case study from central Belgium. *Geomorphology* **118**, 339-348, doi:<https://doi.org/10.1016/j.geomorph.2010.02.001> (2010).
59. Cilek, V. The loess deposits of the Bohemian Massif: silt provenance, palaeometeorology and loessification processes. *Quaternary International* **76-77**, 123-128, doi:[https://doi.org/10.1016/S1040-6182\(00\)00096-3](https://doi.org/10.1016/S1040-6182(00)00096-3) (2001).
60. Smalley, I. J. *et al.* The formation of loess deposits in the Tashkent region and parts of Central Asia; and problems with irrigation, hydrocollapse and soil erosion. *Quaternary International* **152-153**, 59-69, doi:<https://doi.org/10.1016/j.quaint.2005.12.002> (2006).
61. Li, Y. Relationship between the permeability and the porosity of luochuan's loess layer. *J Xi'an Coll Geo* **13**, 60-64, doi:10.19814/j.jese.1991.02.011 (1991).
62. Li, G. & Yang, J. Methods and equipment for the determination of pore size in rocks. China patent (2019).
63. Li, G. & Yang, J. A method for pore and pore throat identification based on 3D core scanning image. China patent (2018).
64. An, Z. *et al.* The long-term paleomonsoon variation recorded by the loess-paleosol sequence in Central China. *Quaternary International* **7-8**, 91-95, doi:[https://doi.org/10.1016/1040-6182\(90\)90042-3](https://doi.org/10.1016/1040-6182(90)90042-3) (1990).
65. Hao, Q. & Guo, Z. Spatial variations of magnetic susceptibility of Chinese loess for the last 600 kyr: Implications for monsoon evolution. *Journal of Geophysical Research: Solid Earth* **110**, doi:<https://doi.org/10.1029/2005JB003765> (2005).
66. Li, Y., Zhang, W., He, S. & Aydin, A. Wetting-driven formation of present-day loess structure. *Geoderma* **377**, 114564, doi:<https://doi.org/10.1016/j.geoderma.2020.114564> (2020).
67. Smalley, I. J. *et al.* The formation of loess deposits in the Tashkent region and parts of Central Asia; and problems with irrigation, hydrocollapse and soil erosion. *Quaternary International* **152-153**, 59-69, doi:<https://doi.org/10.1016/j.quaint.2005.12.002> (2006).
68. Zuo, L., Xu, L., Baudet, B. A., Gao, C. & Huang, C. The structure degradation of a silty loess induced by long-term water seepage. *Engineering Geology* **272**, 105634, doi:10.1016/j.enggeo.2020.105634 (2020).

Figures

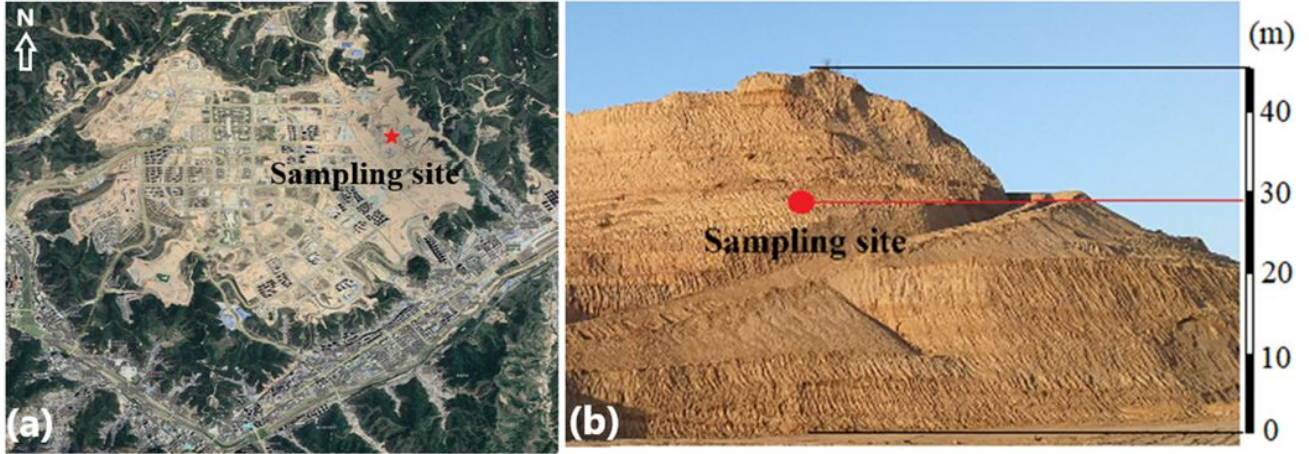


Figure 1

Location of the sampling site: (a) satellite image from google earth of the study area; (b) the excavated slope profile.

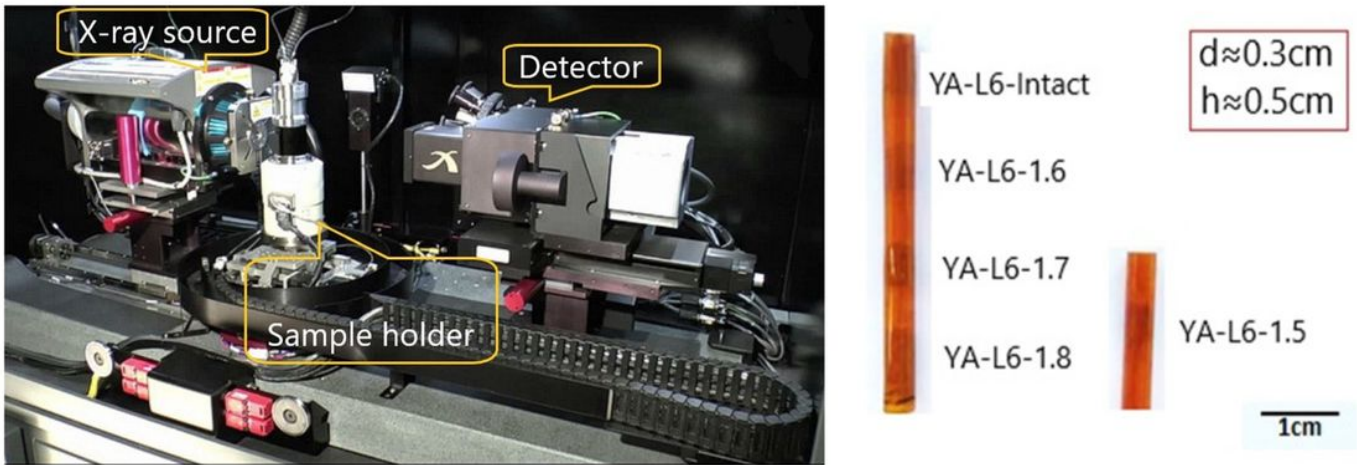


Figure 2

The micro-CT scanner and specimens.

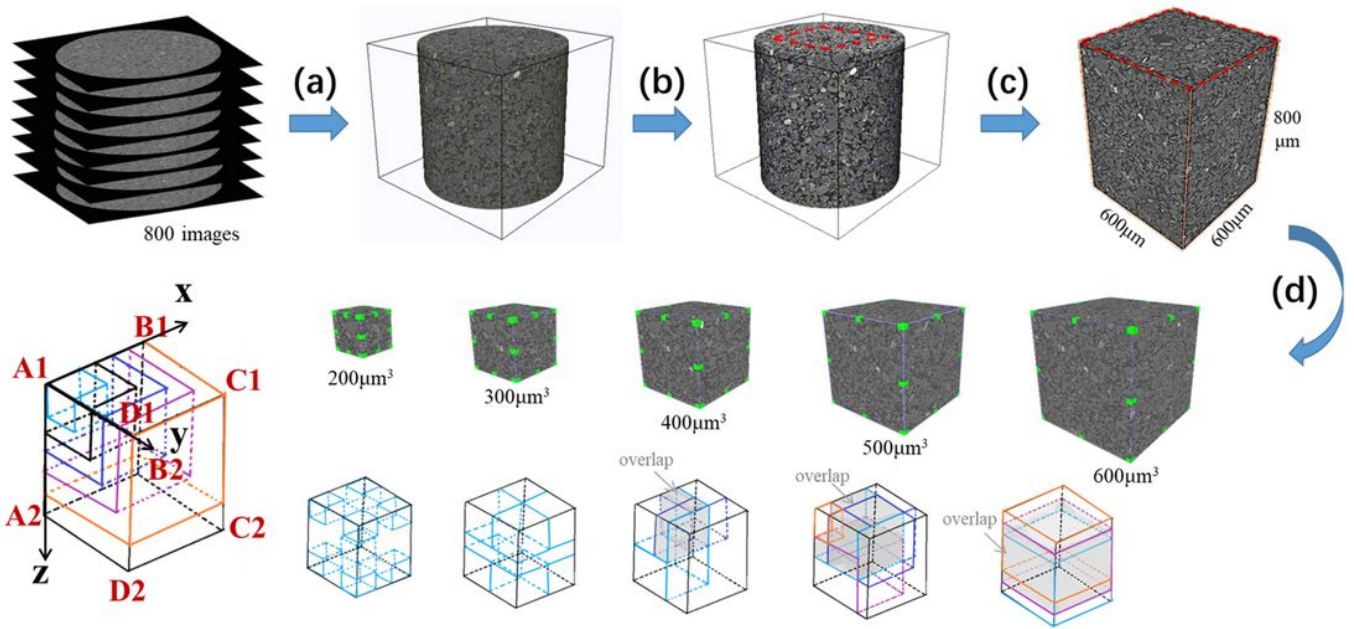


Figure 3

Workflow to generate the cubes to be analyzed: (a) 3D reconstruction; (b) noise reduction; (c) cubic region selection; (d) extract cubes of different sizes.

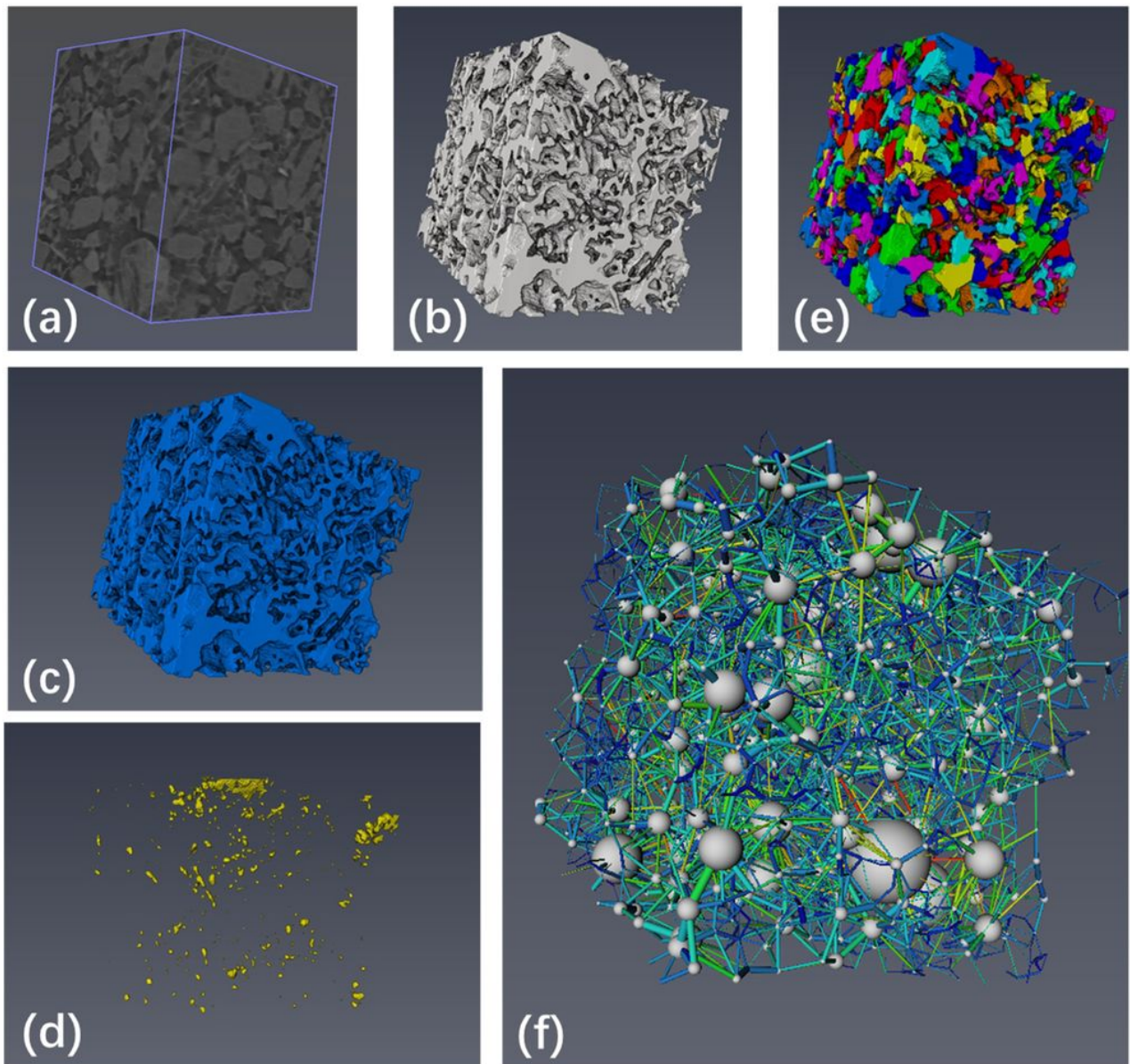


Figure 4

Main steps to get the quantitative parameters:(a) a selected cube; (b) pore microstructure;(c) connected pores; (d) isolated pores; (e) pore space separation; (f) pore network.

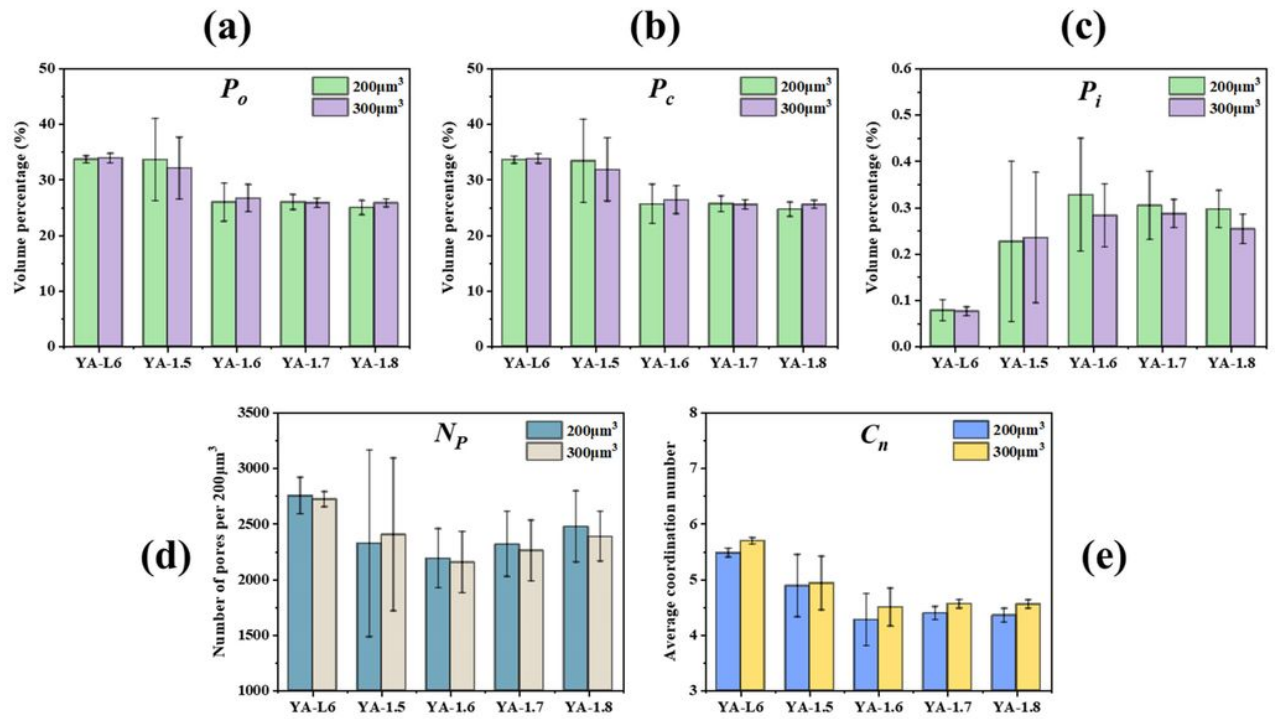


Figure 5

The mean values and standard deviations of parameters of different size cubes of the intact loess (YA-L6) and the compacted loess (YA-1.5, YA-1.6, YA-1.7, YA-1.8): (a) porosity; (b) connected porosity; (c) isolated porosity; (d) number of pores per 200 μm^3 ; (e) average coordination number.

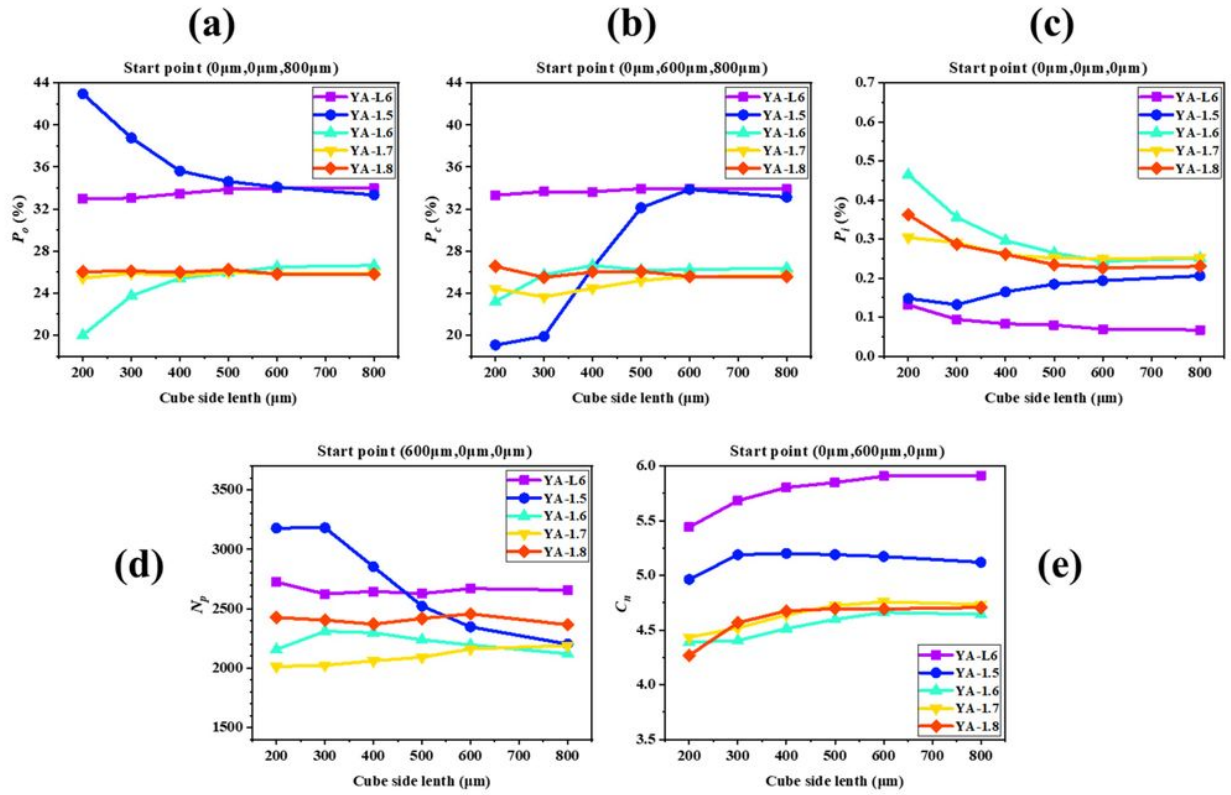


Figure 6

Value of parameters with variation of cube side length, (a)–(e) represents different parameters, start point represents different sub-volume selection schemes.

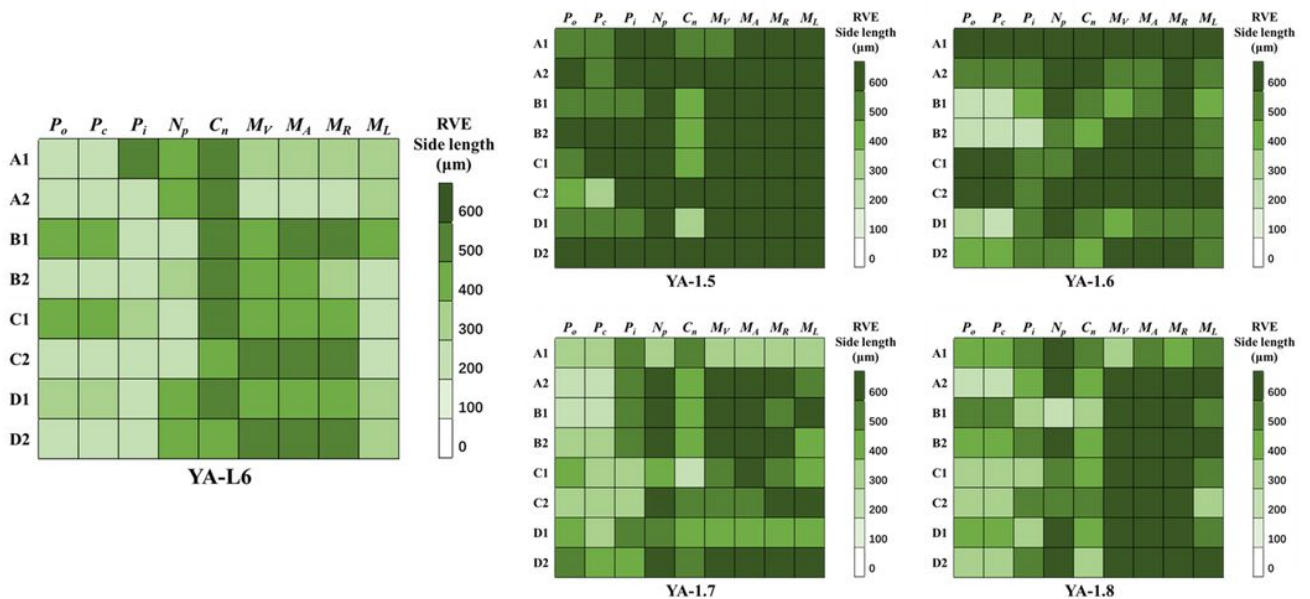


Figure 7

The RVE side lengths based on different parameters of the intact loess (YA-L6) and the compacted loess (YA-1.5, YA-1.6, YA-1.7, YA-1.8), A1-D2 represents different sub-volume selection schemes.

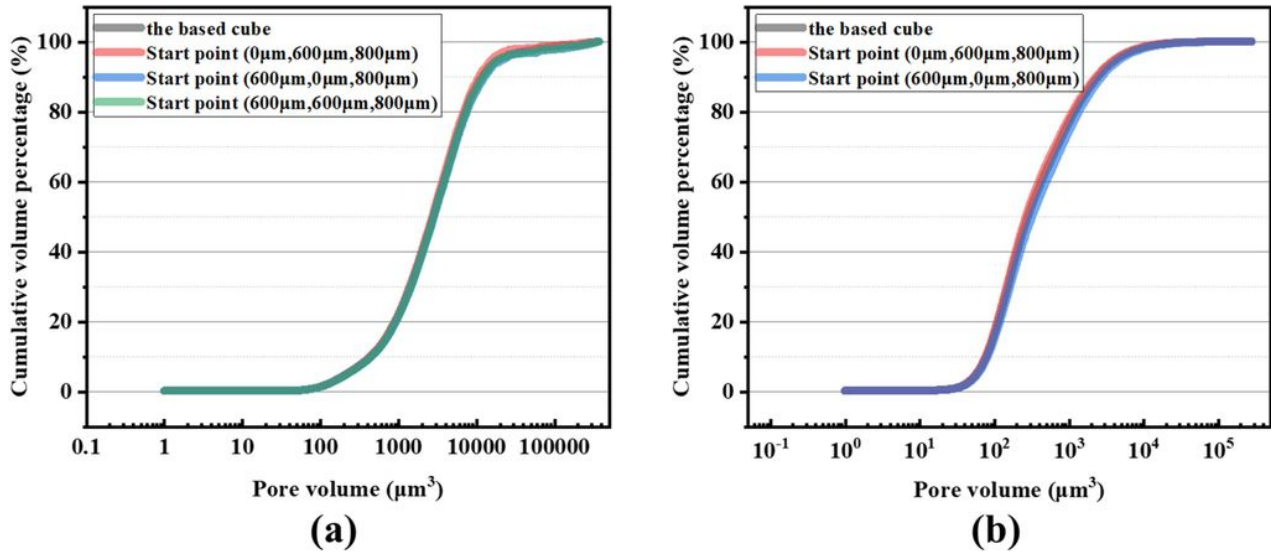


Figure 8

Correlation accumulative curves of the ROI cube and the geometrical RVE cubes: (a) the intact loess; (b) the compacted loess. (Start point represents different sub-volume selection schemes).

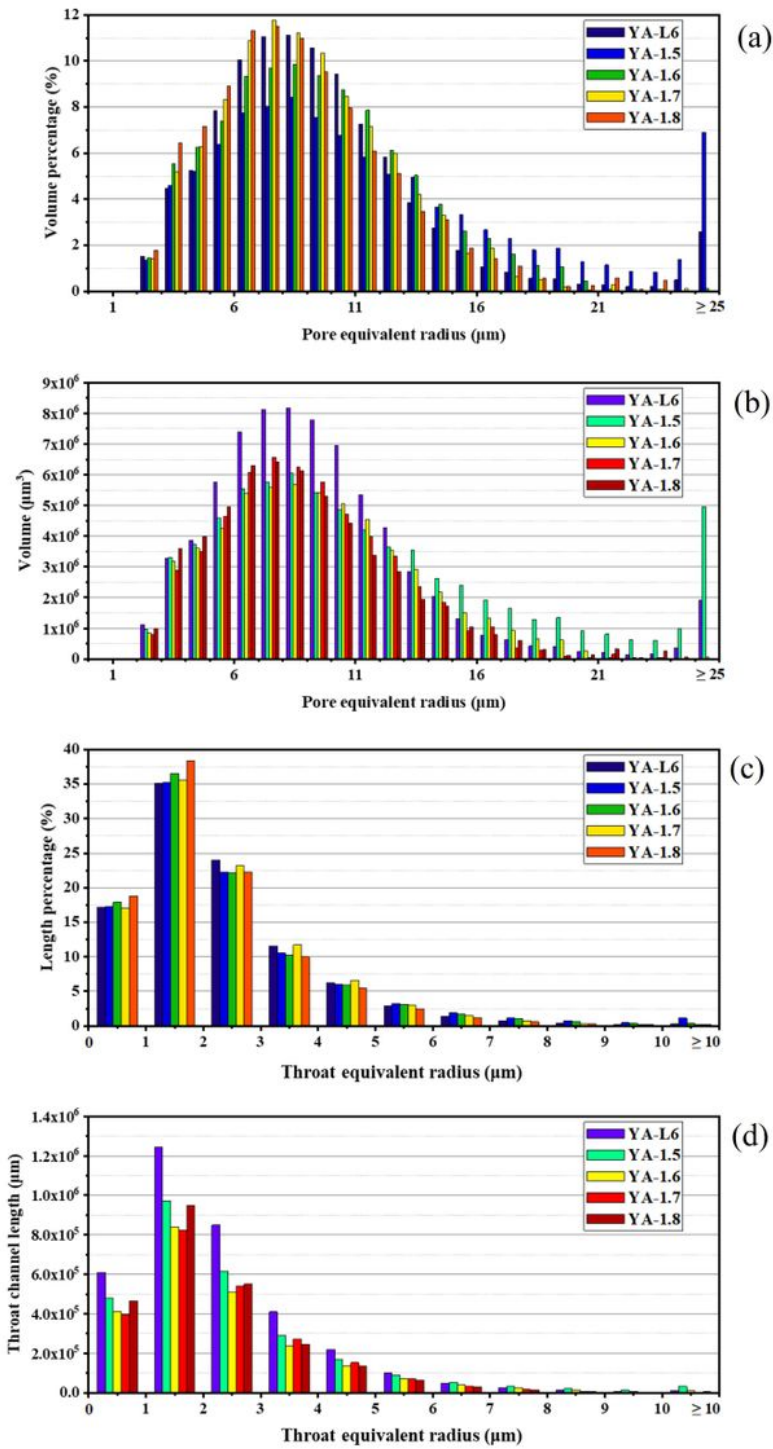


Figure 9

Pore equivalent radius and throat equivalent radius distributions based on the geometrical RVE cubes ($600\mu\text{m}^3$) of the intact loess and the compacted loess: (a) volume percentage of pores at different equivalent pore radius; (b) total volume of pores at different equivalent pore radius; (c) length percentage of throats at different equivalent throat radius; (d) total length of throats at different equivalent throat radius.